Applied Surface Science 540 (2021) 148401

Contents lists available at ScienceDirect

Applied Surface Science

journal homepage: www.elsevier.com/locate/apsusc

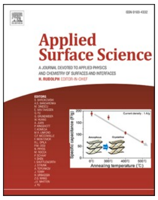

Magnetically separable Z-scheme FeSiB metallic glass/g-C_3N_4 heterojunction photocatalyst with high degradation efficiency at universal pH conditions

Fang Miao [a,1], Qianqian Wang [a,1], Lai-Chang Zhang [b,*], Baolong Shen [a,c,*]

[a] School of Materials Science and Engineering, Jiangsu Key Laboratory for Advanced Metallic Materials, Southeast University, Nanjing 211189, China
[b] School of Engineering, Edith Cowan University, 270 Joondalup Drive, Joondalup, Perth, WA 6027, Australia
[c] Institute of Massive Amorphous Metal Science, China University of Mining and Technology, Xuzhou 221116, China

ARTICLE INFO

Keywords:
G-C_3N_4
FeSiB metallic glass
Heterojunction
Z-scheme photocatalyst
Dye degradation

ABSTRACT

Synthesizing efficient catalysts to degrade hazardous pollutants in wastewater, especially in alkaline conditions, is pivotal for water remediation. A magnetically separable Z-scheme FeSiB metallic glass (MG)/g-C_3N_4 photocatalyst with high activity under visible-light irradiation is prepared via ball milling. The photocatalyst exhibits a sufficient degrading capability to acid orange 7 (AO7) in acidic, neutral and alkaline solutions, and also shows excellent reusability. The photocatalytic efficiency of the composite can be optimized by modifying the weight ratio of FeSiB MG and g-C_3N_4 powders. Heterojunction structure is formed at the interface of g-C_3N_4 and FeSiB MG due to the shearing stress from ball milling, leading to the improvement of the separation efficiency of the photo-generated electron-hole pairs. This results in the enhancement in photocatalytic activity for the composite. Besides, the FeSiB MG/g-C_3N_4 photocatalyst can be recycled from solution conveniently due to their high saturation magnetization. This study offers a magnetically separable photocatalyst that can degrade azo dyes at universal pH conditions.

1. Introduction

Azo dyes are widely used in printing and dyeing industry, and cause serious environmental problems as their azo bonds are strong and difficult to be decomposed naturally [1]. Different kinds of materials, including zero-valent iron (ZVI), bimetallic nanoparticles, metal oxide semiconductor photocatalysts, etc., have been developed to degrade hazardous pollutants, especially azo dyes, from wastewater [2,3]. Most of these materials have several shortcomings, such as difficulty in storage, limited reusability and efficiency. Recently, metallic glasses (MGs), which have a short-range ordered and long-range disordered atomic structure, are widely reported to be promising catalytic materials for wastewater remediation [4,5]. The excellent catalytic property originates from their thermodynamically unstable nature and a large amount of active reaction sites on the surface [6]. Specifically, Fe-based MGs have attracted the most research attentions due to their low-cost and high efficiency [1]. Fe-based MGs have been reported for their efficient degradation and good reusability for a large variety of pollutants, including azo dyes, arsenic and nitrate [7–9]. The FeSiB MGs show efficient electron transfer capability to generate hydroxyl radicals (•OH) for dye degradation due to their randomly packing structure with weak atomic bonding [10]. FeCrNiMoWSiB MG matrix composite manufactured by selective laser melting shows a remarkable catalytic reusability up to 45 times in sulphate radical-based reaction due to their extremely low surface decay [11]. Annealing the MGs to induce formation of multiphase nanocrystals can bring a compelling rejuvenation in the catalytic efficiency in Fe-based MGs [5,12]. However, there is still presenting great impedances of Fe-based MGs before they can be industrially applied in wastewater remediation largely because of their limited catalytic efficiency. Besides, the Fe-based MGs reported up to date mostly degrade pollutants through Fenton-like or reduction reactions, which are only effective in acid or neutral wastewater [13,14]. Improving the degradation efficiency of Fe-based MGs in alkaline solutions is also important.

---

[*] Corresponding authors at: School of Materials Science and Engineering, Jiangsu Key Laboratory for Advanced Metallic Materials, Southeast University, Nanjing 211189, China (B. Shen).

E-mail addresses: lczhangimr@gmail.com, l.zhang@ecu.edu.au (L.-C. Zhang), blshen@seu.edu.cn (B. Shen).

[1] These authors contributed equally.

https://doi.org/10.1016/j.apsusc.2020.148401
Received 11 August 2020; Received in revised form 23 October 2020; Accepted 5 November 2020

Furthermore, graphite carbonitride (g-C_3N_4) is a well-known semiconductor photocatalyst. The g-C_3N_4 shows high photocatalytic activity and good reusability due to its narrow band gap (2.7 eV) and high chemical and thermal stability [15–18]. However, the fast recombination of photo-generated electron-hole pairs, as well as poor absorption of visible-light irradiation, decreases the photocatalytic efficiency of g-C_3N_4 [19–21]. Moreover, the reliability is also a bottle-neck problem for g-C_3N_4 powders. Some composites, including Ag_2S/K-g-C_3N_4 [22], Ag_3PO_4/P-g-C_3N_4 [23], and g-C_3N_4/$Bi_4O_5I_2$ [24], have been synthesized to overcome the shortcomings of g-C_3N_4. Among them, the magnetically separable crystalline iron oxides/g-C_3N_4 composites, such as Fe_2O_3/g-C_3N_4 and Fe_3O_4/g-C_3N_4, not only facilitate the recycle of g-C_3N_4 powders, but also enhance the photocatalytic performance by accelerating the separation of electron-hole pairs, encouraging the interfacial charge transfer, and increasing adsorption of visible-light irradiation[19,25]. As Fe-based MGs contain a large amount of unsaturated ZVI on the surface, Fe-based MG/g-C_3N_4 composites should have better photocatalytic performance. However, rare report about MG/g-C_3N_4 composite has been made. Besides, the arrangement of atoms in amorphous matrix is completely different from the arrayed atoms in crystalline alloys [6]. How the unsaturated ZVI in amorphous matrix affect the atomic configuration and electronic structure at the interface between MG and the semiconductor material remains uncovered. How this unique MG/semiconductor material interface affects the charge transfer, vacancy construction and light adsorption, and thus contributing to the photocatalytic activity is still a very challenge field.

In addition, g-C_3N_4 is commonly used as a platform to build Z-scheme catalytic systems because of its high specific surface area and low charge recombination rate [26]. The Z-scheme junction is one kind of photocatalysts with heterojunction structures, and it can simultaneously possess the wide light-absorption range, strong redox ability, and efficient separation efficiency of photo-generated carriers [27–29]. Many Z-scheme hybrid photocatalytic systems have been successfully constructed and show satisfactory photocatalytic efficiency under visible light, such as BiOI/g-C_3N_4 [30], $CuBi_2O_4$/WO_3 [31], TiO_2/g-C_3N_4 [32], g-C_3N_4/ZnO [33], CdS/$Co_{1-x}S$ [34], and $MgTi_2O_5$/g-C_3N_4 [35]. Motivated by the above works, we tend to construct a magnetically separable MG/g-C_3N_4 composite with Z-scheme heterojunction structure that can facilitate dye degradation efficiently and uncovers the photocatalytic pathway for this composite.

$Fe_{78}Si_9B_{13}$ MG, which has been produced in an industrial-scale due to their excellent soft magnetic properties, shows superb capabilities in degrading organic contaminants in wastewater [36,37]. Previous researches have proved that ball milling is an effective method to introduce the structure disorder, vacancy and surface defects into materials [38], which has the potential to offer active sites for trapping photo-induced carriers and also reduce the recombining rate of electron-hole pairs, and thus improving the catalytic activity. Thus, in this work, we facilely ball milled g-C_3N_4 powders and $Fe_{78}Si_9B_{13}$ MG powders to synthesize FeSiB MG/g-C_3N_4 photocatalysts, and evaluate their catalytic performance through the degradation of acid orange 7 (AO7) dye. The photocatalytic efficiency of the FeSiB MG/g-C_3N_4 composites can be optimized by modifying the FeSiB MG/g-C_3N_4 ratio. The composite can degrade AO7 efficiently at pH ranging from 2 to 10, showing prominent environmental adaptability. Besides, the FeSiB MG/g-C_3N_4 composite exhibits superior saturation magnetization that can facilitate the recycle process. Heterojunction structure is formed at the interface of FeSiB MG/g-C_3N_4, leading to the increase of the separation efficiency of electron-hole pairs.

2. Materials and methods

2.1. Materials

Alloy ingots with a nominal composition of $Fe_{78}Si_9B_{13}$ (in atomic percentage) were made by arc melting the raw materials of Fe (99.99 wt %), Si (99.99 wt%), and B (99.99 wt%) in a purified argon atmosphere. FeSiB MG powders were fabricated using a high pressure argon gas atomization system, where induction heating was employed to melt the ingots and then the melts were injected through a nozzle with a 0.8 mm diameter under flowing argon gas, which had a dynamic pressure measured at 0 to 8 MPa.

The g-C_3N_4 powders were synthesized according to the previous reported procedures [39]. Specifically, 6 g of melamine powders were placed into an alumina crucible, which was subsequently calcined at 823 K for 4 h with a heating rate of 5 K/min. After cooling down to room temperature, the received g-C_3N_4 bulk was ground into powders. The sodium hydroxide (NaOH) used in this work was purchased from Greagent. The sulphuric acid (H_2SO_4) was provided by Chron Chemicals. The acid orange 7 ($C_{16}H_{11}N_2NaO_4S$, AO7) was procured from Xiya Reagent. The *tert*-butylalcohol ($C_4H_{10}O$), benzoquinone ($C_6H_4O_2$) and sodium oxalate ($Na_2C_2O_4$) were provided by Sinopharm Chemical Reagent Co., Ltd. All the above regents were in AR grade.

To synthesize the FeSiB/g-C_3N_4 heterojunction photocatalyst, 5 g mixture of FeSiB and g-C_3N_4 powders were added into a zirconia ball milling pot with 3 mL ethanol then milled at 500 revolutions per minute (rpm) for 3 h. The mass ratio of FeSiB MG powders to g-C_3N_4 powders of 1/4, 1/2, 1/1, 3/2 and 2/1 was separately adopted, with the obtained samples hereafter denoted as FeSiB/g-C_3N_4-1/4, FeSiB/g-C_3N_4-1/2, FeSiB/g-C_3N_4-1/1, FeSiB/g-C_3N_4-3/2 and FeSiB/g-C_3N_4-2/1, respectively. For comparison, the Fe_3O_4/g-C_3N_4 composite is also prepared in the same way for the FeSiB/g-C_3N_4-3/2 sample.

2.2. Characterization

The curves of magnetization were measured in a changing magnetic field ranging from −740 to 740 Oe on a Lake Shore 7407 vibrating sample magnetometer (VSM). X-ray diffraction (XRD) patterns of all samples were obtained using a Bruker D8 Advance X-ray diffractometer. Scanning electron microscopy (SEM) analyses were performed on a FEI Sirion 200 scanning electron microanalyzer with an energy dispersive X-ray spectroscope (EDS). Transmission electron microscopy (TEM) and high resolution transmission electron microscopy (HRTEM) observations were performed on a JEOL JEM2100 microscope with an energy dispersive X-ray (EDX) spectroscopy. The UV–Vis diffuse reflectance spectrum (DRS) was performed using a Hitachi UV-3010 spectrophotometer, utilizing $BaSO_4$ as a functional reference. Photoluminescence (PL) spectra of all the samples were collected utilizing Varian Cary Eclipse spectrophotometer at 325 nm excitation wavelength. The Brunauer-Emmett-Teller (BET) surface area was determined by nitrogen adsorption desorption on an ASAP 2460 analyzer. The X-ray photoelectron spectroscopy (XPS) was conducted on a PHI 5300 ESCA system with Al Kα (1486.6 eV) X-ray source to investigate the binding energies of the elements of the surfaces. The charge calibration was carried out using C 1 s (284.80 eV) as charge compensation. About 20–30 mg powder was fixed on the sample stage with conductive tapes for each XPS test. The band energy of FeSiB MG was measured using ultraviolet photoelectron spectroscopy (UPS) on a PHI 5000 ESCA system with the pass energy of 2.60 eV and sample bias of 0 V.

Photoeletrochemical measurements were performed using an electrochemical workstation (CHI660E, Shanghai, China) under a three-electrode system. Moreover, the Ag/AgCl electrode, Pt foil, and the photocatalyst were utilized as the reference electrode, counter electrode, and working electrode, respectively. To prepare the working electrode, 1 mg photocatalyst was dispersed in 1 mL ethanol containing 40 μL Nafion with sonication. Then, 20 μL of the above solution was dropped onto ITO glass ($20 \times 20 \times 2.3$ mm^3) with an area of 100 mm^2, and then dried at room temperature for 24 h. Before irradiation, 0.1 moL^{-1} Na_2SO_4 solution was inlet with N_2 to remove the gas dissolved in electrolyte. The transient photocurrent response and electrochemical impedance spectroscopy (EIS) characterization tests were conducted in an irradiation reaction vessel using a UV–visible light (PLS-SXE 300D/

300DUV, Beijing Perfectlight).

2.3. *Photocatalytic activity*

The photocatalytic performance of all the as-prepared samples were evaluated via the degradation of AO7 under visible-light irradiation. UV–visible light was used as the source of visible light. In a typical photocatalytic measurement, 250 mL (20 mg/L if not noted) AO7 solution was made using deionized water in a 500 mL beaker. The pH (pH = 7 if not noted) of the solution was adjusted using 1 mol/L NaOH and 5% H_2SO_4. A water bath was used to maintain the temperature of the solution ($T = 298$ K if not noted). A certain amount of photocatalysts (1 g/L if not noted) were added into the solution, which was then stirred mechanically at a fixed speed of 120–130 r/min. At selected time intervals, 3 mL of the solution was drawn up using a syringe and then the absorbance of filtered supernatants was measured by UV–Vis spectrophotometry. In terms of cyclic tests, the powders after each of the degradation experiments were extracted from the aqueous solution with a magnet, and then cleaned with deionized water for 20 s before the next cycle. Additionally, to carry out the active species trapping experiments, the $C_4H_{10}O$, $C_6H_4O_2$ and $Na_2C_2O_4$ were introduced to the reaction system as scavengers of •OH, $\bullet O_2^-$ and h^+, respectively.

3. Results and discussion

3.1. *Microstructure of the photocatalysts*

Fig. 1 is the schematic illustration for the synthesizing process of FeSiB/g-C_3N_4 composites. The FeSiB and g-C_3N_4 powders are ball-milled to form the composites with a heterojunction structure. Fig. 2a shows the XRD patterns of the as-received FeSiB and g-C_3N_4 powders. The FeSiB powders display only a broad diffuse diffraction characteristic at $2\theta = 45^\circ$ without any detectable sharp peak on its XRD pattern, suggesting an amorphous feature. The XRD pattern of g-C_3N_4 powders has a strong and distinct diffraction peak at $2\theta = 27.5^\circ$, representing the typical interlayer-stacking peak (0 0 2) with an interlayer gap of ~ 0.326 nm for g-C_3N_4 [40]. All the XRD patterns of ball-milled FeSiB/g-C_3N_4 composites with different FeSiB contents (Fig. 2b) match well with the corresponding peaks from g-C_3N_4 and FeSiB powders, implying the successful synthesis of the FeSiB/g-C_3N_4 composites. It is noted that the intensities of diffraction peak of g-C_3N_4 at 27.5° decrease gradually with increasing the FeSiB content. Similar results have also been found in the preparation of Fe_2O_3/g-C_3N_4 photocatalysts [25], where the intensities of diffraction peak at 27.5° became weaker as Fe_2O_3 content increased. This phenomenon suggests that the crystallization of g-C_3N_4 is gradually inhibited with the introduction of FeSiB MG powders.

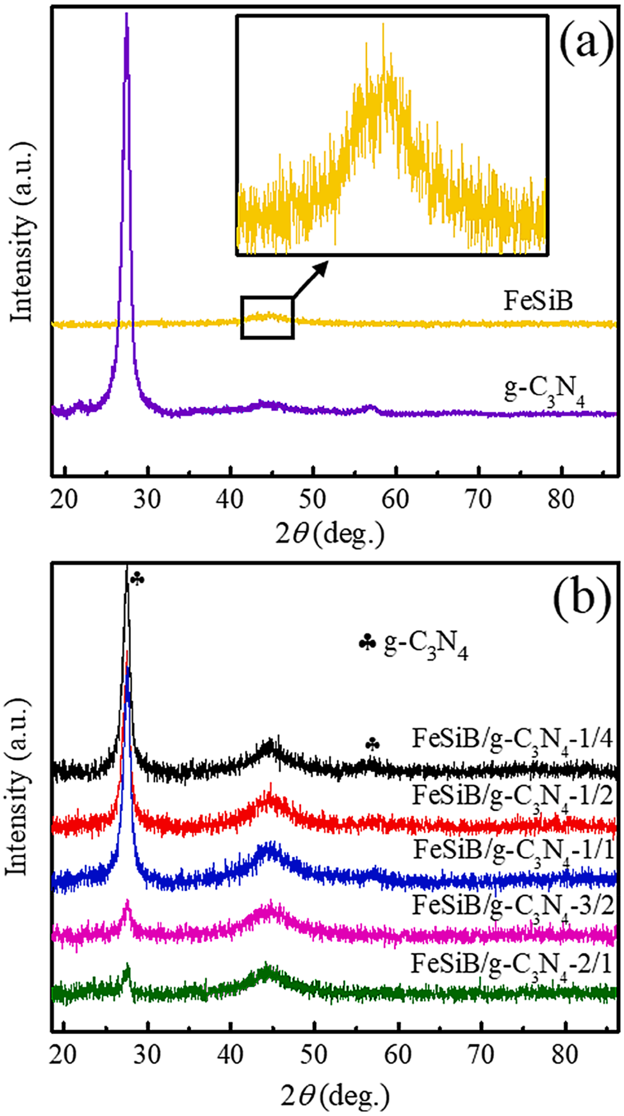

Fig. 2. XRD patterns of (a) FeSiB and g-C_3N_4 powders, (b) FeSiB/g-C_3N_4-1/4, 1/2, 1/1, 3/2, 2/1 photocatalysts.

3.2. *Photocatalytic and magnetic properties*

The UV–Vis absorbance spectra of the filtered AO7 solutions are recorded after adding the photocatalysts at different reaction time, as shown in Fig. 3a-d. The maximum adsorption peak at 485 nm arising

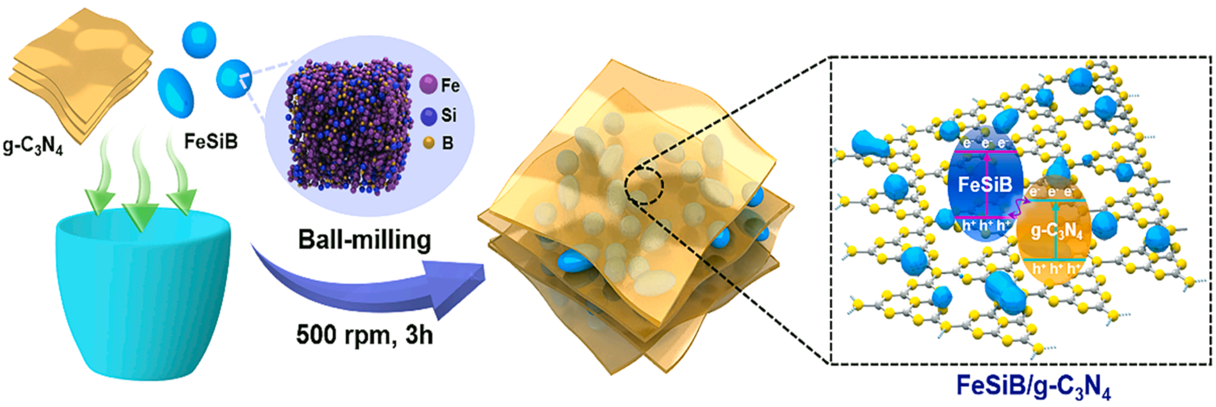

Fig. 1. A schematic illustration for facile fabrication of the FeSiB/g-C_3N_4 photocatalyst.

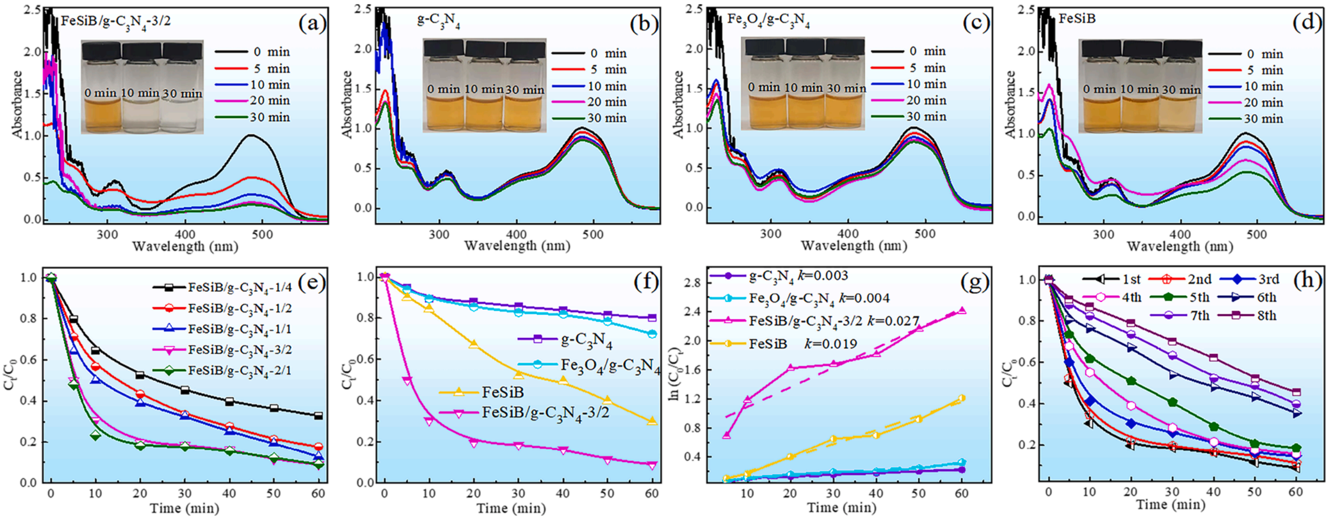

Fig. 3. UV–Vis absorbance spectra of AO7 solutions during the photocatalysis using (a) FeSiB/g-C_3N_4-3/2, (b) g-C_3N_4, (c) Fe_3O_4/g-C_3N_4, (d) FeSiB, insets are visible color change of AO7 solution. Normalized concentration change of AO7 solution during the photocatalysis using (e) FeSiB/g-C_3N_4-1/4, 1/2, 1/1, 3/2, 2/1 and (f) g-C_3N_4, Fe_3O_4/g-C_3N_4, FeSiB, FeSiB/g-C_3N_4-3/2 photocatalysts. (g) The ln (C_0/C_t) *vs.* time curves of g-C_3N_4, Fe_3O_4/g-C_3N_4, FeSiB, and FeSiB/g-C_3N_4-3/2 photocatalysts. (h) Normalized concentration change of AO7 solution at different degradation cycles during the photocatalysis using FeSiB/g-C_3N_4-3/2 photocatalysts.

from the azo chromophore of AO7 is proportional to the dye concentration in solution. This peak becomes weak as the reaction time increases, indicating the decolorization of AO7. The concentration of the solution using the FeSiB/g-C_3N_4-3/2 photocatalyst decreases significantly within the first 10 min, while the catalysts of g-C_3N_4, Fe_3O_4/g-C_3N_4 and FeSiB present a much slower performance. The color changes of the solutions shown in the insets of Fig. 3a-d further confirm the exceptional degradation efficiency of the FeSiB/g-C_3N_4-3/2 photocatalyst. The solution is almost clear after degradation by the FeSiB/g-C_3N_4-3/2 photocatalyst for 10 min; by contrast, the solution retains yellow after degradation for 10 min when employing the catalysts of g-C_3N_4, Fe_3O_4/g-C_3N_4 and FeSiB, respectively.

Fig. 3e shows the normalized concentration changes of the AO7 solution in the process of degradation using FeSiB/g-C_3N_4-1/4, 1/2, 1/1, 3/2, 2/1 photocatalysts. By increasing the FeSiB content, the time required to decompose 80% AO7 using the FeSiB/g-C_3N_4 photocatalysts becomes gradually shorter. However, there is a limit for the improvement of the degradation efficiency with increasing the FeSiB content, as evidenced by the same amount of time for degradation by FeSiB/g-C_3N_4-3/2 and FeSiB/g-C_3N_4-2/1. Thus, the FeSiB/g-C_3N_4-3/2 is considered as the optimized composition to degrade AO7. Fig. 3f compares the normalized concentration changes of the AO7 solution in the process of degradation using g-C_3N_4, Fe_3O_4/g-C_3N_4, FeSiB and FeSiB/g-C_3N_4-3/2. It is evident that 80% of AO7 is removed after 20 min irradiation using the FeSiB/g-C_3N_4-3/2 photocatalyst, while more than 50% of AO7 remain in the solutions that using g-C_3N_4, Fe_3O_4/g-C_3N_4 or FeSiB. This indicates that the FeSiB/g-C_3N_4-3/2 photocatalysts possess superior photocatalytic capability compared with g-C_3N_4, Fe_3O_4/g-C_3N_4 and FeSiB samples.

The curves of the normalized concentration change of the AO7 degradation using g-C_3N_4, Fe_3O_4/g-C_3N_4, FeSiB and FeSiB/g-C_3N_4-3/2 photocatalysts are in line with the pseudo-first-order kinetic model. To investigate quantitatively the reaction kinetics, the reaction rate constant (*k*) is calculated based on Equation (1):

$$\ln\left(\frac{C_0}{C_t}\right) = kt \tag{1}$$

where *k* is the reaction rate constant ($\min^{-1}$), C_0 and C_t are the initial of concentration and the instantaneous concentration at time *t* for the AO7 solution respectively. Accordingly, the curves of ln (C_0/C_t) *vs.* time are shown in Fig. 3g. The *k* of AO7 degradation using FeSiB/g-C_3N_4-3/2 photocatalysts (0.027 $\min^{-1}$) is 9.0, 6.8 and 1.4 times that of g-C_3N_4 (0.003 $\min^{-1}$), Fe_3O_4/g-C_3N_4 (0.004 $\min^{-1}$), and FeSiB (0.019 $\min^{-1}$), respectively, in the same experimental conditions. These results demonstrate that the photocatalytic capability of g-C_3N_4 can be efficiently enhanced by introducing FeSiB under visible-light irradiation. Based on the results shown above, the FeSiB/g-C_3N_4-3/2 photocatalyst exhibits an excellent ability to degrade AO7 solution in the photocatalytic reaction.

In addition, Fig. 3h shows the reusability of the representative composite photocatalysts (FeSiB/g-C_3N_4-3/2). All the photocatalytic reactions using FeSiB/g-C_3N_4-3/2 photocatalysts can achieve 80% decomposition of AO7 in less than 50 min in the first 5 cycles, suggesting that the FeSiB/g-C_3N_4-3/2 photocatalysts can be recycled for at least 5 times before obvious deactivation of the photocatalytic activity. The 6th cycle shows a slow degradation rate, decomposing only 55% of AO7 within 50 min. To analyze the reasons for the decline of photocatalytic activity, the content of elements on the surfaces of FeSiB/g-C_3N_4-3/2 before and after the 5th cycle are analyzed by EDS, and the data are summarized in Table 1. The amount of oxygen on the surface of FeSiB/g-C_3N_4-3/2 before reaction is too small to be detected by EDS, but sharply increases to 22 at.% on the sample after the 5th reaction cycle. The EDS data confirms that the passivation layer is formed on the surface of FeSiB/g-C_3N_4-3/2 photocatalysts after the 5th reaction cycle. Besides, some literatures indicated that the formed passive layer on the surface of amorphous alloys cause reduction in dye degradation performance [14,41,42]. Thus, the reason for the declined photocatalytic activity after the 5th cycle is formation of the passive layer on the surface of FeSiB/g-C_3N_4-3/2 photocatalysts. Note that, the cycle number reported for the g-C_3N_4 powders or their composite powders to degrade organic compounds is generally 3–5 times. The FeSiB/g-C_3N_4-3/2 photocatalyst synthesized in this work possesses a comparable reusability.

Fig. 4 shows the effect of different pH values (ranging from 2 to 11) on the degradation efficiency for the FeSiB/g-C_3N_4-3/2 photocatalyst. It is clear that the dye degradation efficiency is fast under acid, neutral,

Table 1
EDS analysis of FeSiB/g-C_3N_4-3/2 photocatalysts before reaction and after the 5th reaction cycle (at.%).

Composites	Fe	Si	B	C	N	O
FeSiB/g-C_3N_4-3/2 before reaction	37	3	–	36	24	0
FeSiB/g-C_3N_4-3/2 after reaction	41	2	–	24	11	22

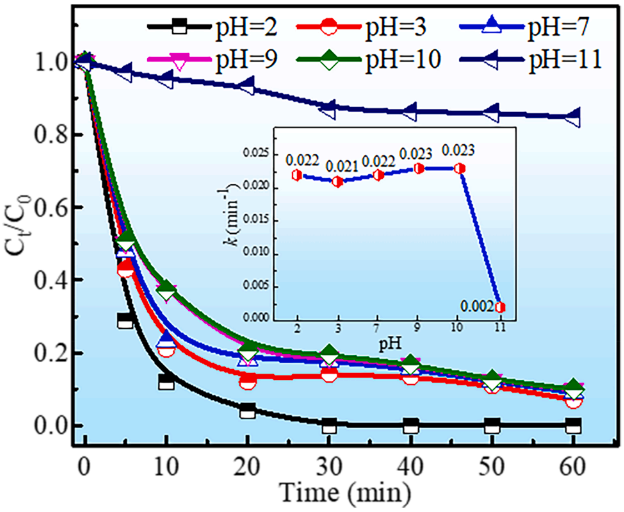

Fig. 4. Effect of pH on the normalized concentration change of AO7 solution during the photocatalytic reaction using FeSiB/g-C_3N_4-3/2 photocatalysts, with inset showing the derived k at different pH.

and alkaline conditions. The 96%, 88%, 82%, 81%, and 80% of AO7 is degraded within 20 min at pH = 2, 3, 7, 9, and 10, respectively. The k of the reactions at different pH shown in the inset of Fig. 4 further confirms that the FeSiB/g-C_3N_4-3/2 photocatalyst has an excellent photocatalytic efficiency at pH ranging from 2 to 10, which makes it suitable for industrial applications. The reasons that FeSiB/g-C_3N_4-3/2 photocatalysts sustain high degradation efficiency at pH ranging from 2 to 10 but not at pH = 11 are as follows. When the initial pH $\leq$ 10 (<pH_{pzc}, pzc stands for the point of zero charge) [43,44], the surface of photocatalyst is still positively charged and the dye molecules with a sulfuric group are negatively charged, which is favourable for their adsorption onto the photocatalyst surface [43,44], and thus the composite still has high degradation efficiency. When pH = 11 (>pH_{pzc}), the photocatalyst surface becomes negatively charged and the surface could be easily covered by corrosion products, which will decrease the number of reactive sites and inhibit the electron transfer [43,44]. Thus, the photocatalytic activity of FeSiB/g-C_3N_4 at pH = 11 is greatly decreased.

Magnetic properties of the synthesized FeSiB/g-C_3N_4 composites are studied and compared with Fe_3O_4/g-C_3N_4 composites at room temperature, as seen in Fig. 5a. Evidently, the FeSiB/g-C_3N_4-3/2 composite exhibits much larger saturation magnetization (M_s) compared with the Fe_3O_4/g-C_3N_4 composite, indicating that the addition of FeSiB powders leads to more improved magnetic properties. Furthermore, the M_s of these composites is enhanced with increasing the FeSiB content in composites. Besides, the inset of Fig. 5a shows that the FeSiB/g-C_3N_4-3/2 composite have lower residual magnetism (M_r) than the Fe_3O_4/g-C_3N_4 composite. This suggests that it is much easier for the FeSiB/g-C_3N_4-3/2 composite to be demagnetized and dispersed in the AO7 solution, which is beneficial for the degradation process. The photos of the FeSiB/g-C_3N_4-3/2 composite powders in deionized water with the magnet applied and removed are shown in Fig. 5b. It shows that the FeSiB/g-C_3N_4-3/2 composite powders can be separated from the solution when applied magnetic field, and then disperse uniformly in the solution after removing the magnetic filed. The above results clearly indicate that the FeSiB/g-C_3N_4-3/2 composite can be an ideal candidate photocatalyst that can be magnetically separable for environmental applications.

3.3. Morphology, electronic structure and optical property of photocatalysts

The morphologies of FeSiB, g-C_3N_4, and FeSiB/g-C_3N_4-3/2 catalysts are analyzed by SEM as shown in Fig. 6. Most of FeSiB MG powders are in ellipsoidal or globular shape (Fig. 6a), while the g-C_3N_4 powders are in small agglomerate and irregular blocks (Fig. 6b). After ball milling the FeSiB powders with the g-C_3N_4 (Fig. 6c and d), a layer of small spheroidal particles is attached uniformly on the surface of large powders, enabling the formation of binary heterostructure. Furthermore, the TEM image of FeSiB/g-C_3N_4-3/2 photocatalyst in Fig. 7a shows the coexistence of two kinds of microstructures, irregular powders wrapped by another phase. The HRTEM image in Fig. 7b confirms both of the phases are amorphous, which is consistent with the characteristics of FeSiB and g-C_3N_4 phases. The EDX mappings of FeSiB/g-C_3N_4-3/2 photocatalyst are provided in Fig. 7c-f. Fe is only detected on the small particles, while C and N are almost homogeneously distributed on the whole bulk. This reveals that the small particles are FeSiB MGs, while the large powders are g-C_3N_4. Based on the above morphological, microstructural and elemental analyses, we propose that the composite is made of FeSiB

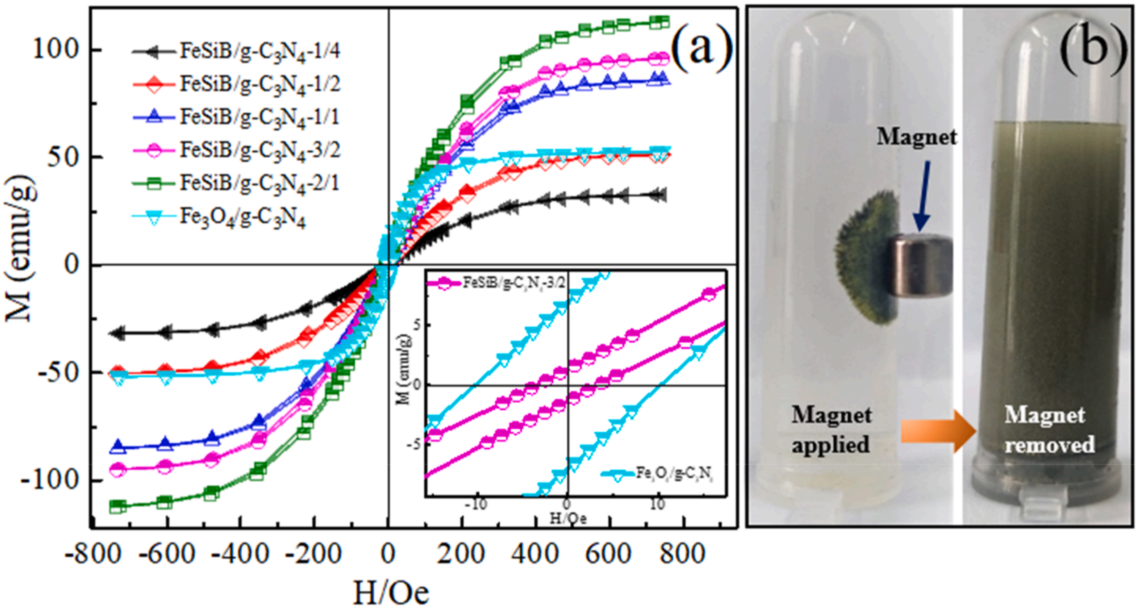

Fig. 5. (a) Magnetization curves of FeSiB/g-C_3N_4-1/4, 1/2, 1/1, 3/2, 2/1 and Fe_3O_4/g-C_3N_4 photocatalysts, with insets showing the residual magnetism (M_r). (b) The FeSiB/g-C_3N_4-3/2 photocatalysts in aqueous solution when applying or removing a magnet.

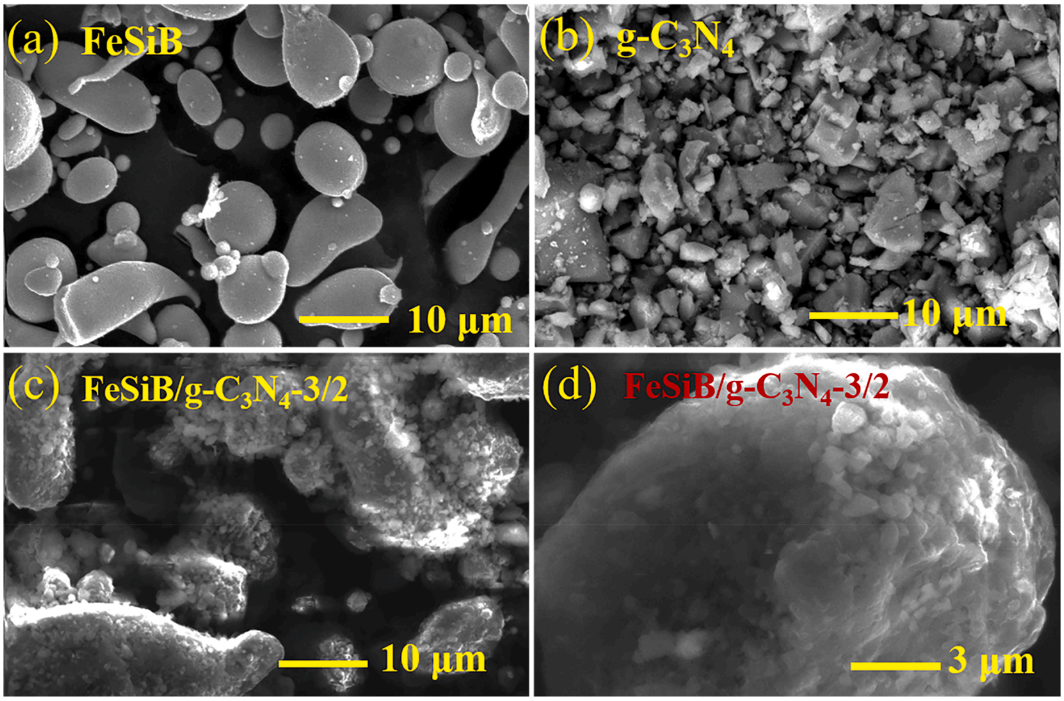

Fig. 6. SEM micrographs of (a) FeSiB powders, (b) g-C_3N_4 powders and (c),(d) FeSiB/g-C_3N_4-3/2 photocatalysts.

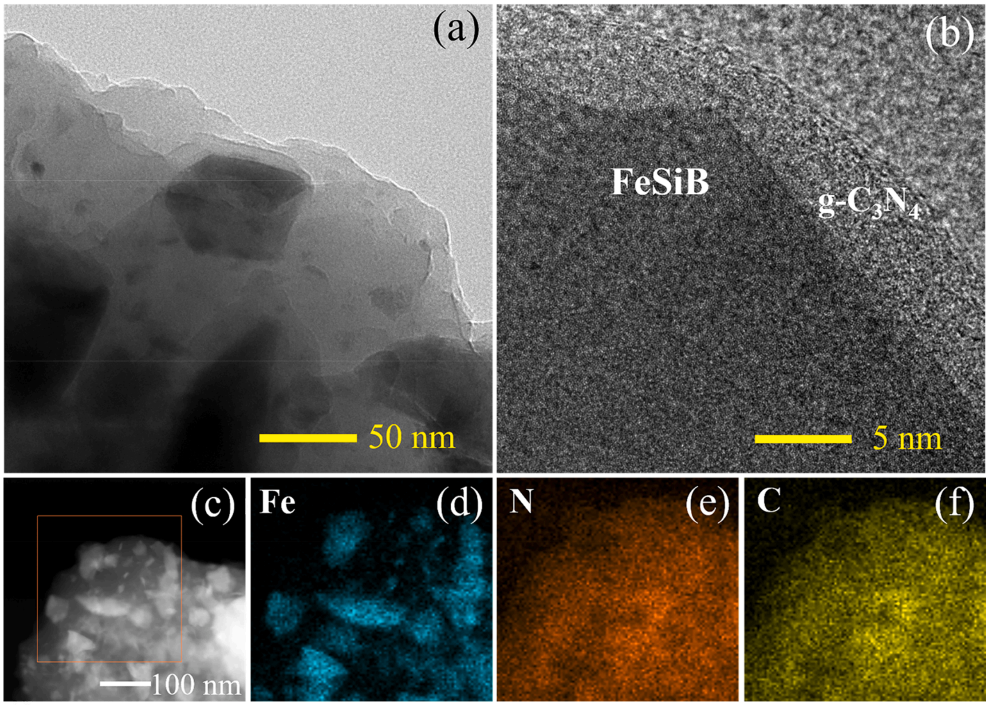

Fig. 7. (a) TEM image of FeSiB/g-C_3N_4-3/2 photocatalysts, (b) HRTEM image of FeSiB/g-C_3N_4-3/2 photocatalysts. (c) TEM image of FeSiB/g-C_3N_4-3/2 photocatalysts. (d)-(f) The EDX mapping of framed sample in (c), showing the elemental distribution of Fe, N and C, respectively.

powders wrapped by g-C_3N_4. Also, at the boundary of FeSiB and g-C_3N_4, heterojunction structure is formed, which can facilitate the transport of photo-generated charge carriers and enhance the photocatalytic activity [45–47].

In order to understand the electronic structures of the g-C_3N_4, FeSiB and the FeSiB/g-C_3N_4-3/2 photocatalysts, XPS analyses were carried out on the samples and the results are shown in Fig. 8. As shown in Fig. 8a, the peaks of the C 1 s spectrum for the g-C_3N_4 can be attributed to C–C (284.47 eV) and C-N_3 (287.90 eV) [48–50]. The binding energy values for C 1 s in the FeSiB/g-C_3N_4-3/2 photocatalyst are observed at 285.02 eV and 288.35 eV, which present a slight positive shift compared with those for g-C_3N_4. The peaks of the N 1 s spectrum for the g-C_3N_4 shown in Fig. 8b can be attributed to C-N-C (398.37 eV), N-C_3 (400.17 eV) [48–52], and charging effects (404.43 eV) [49,51,52]. For FeSiB/g-C_3N_4-3/2, these three peaks shift slightly to 398.98 eV, 400.97 eV, and 404.89 eV, respectively. As the binding energies of C 1 s and N 1 s shift

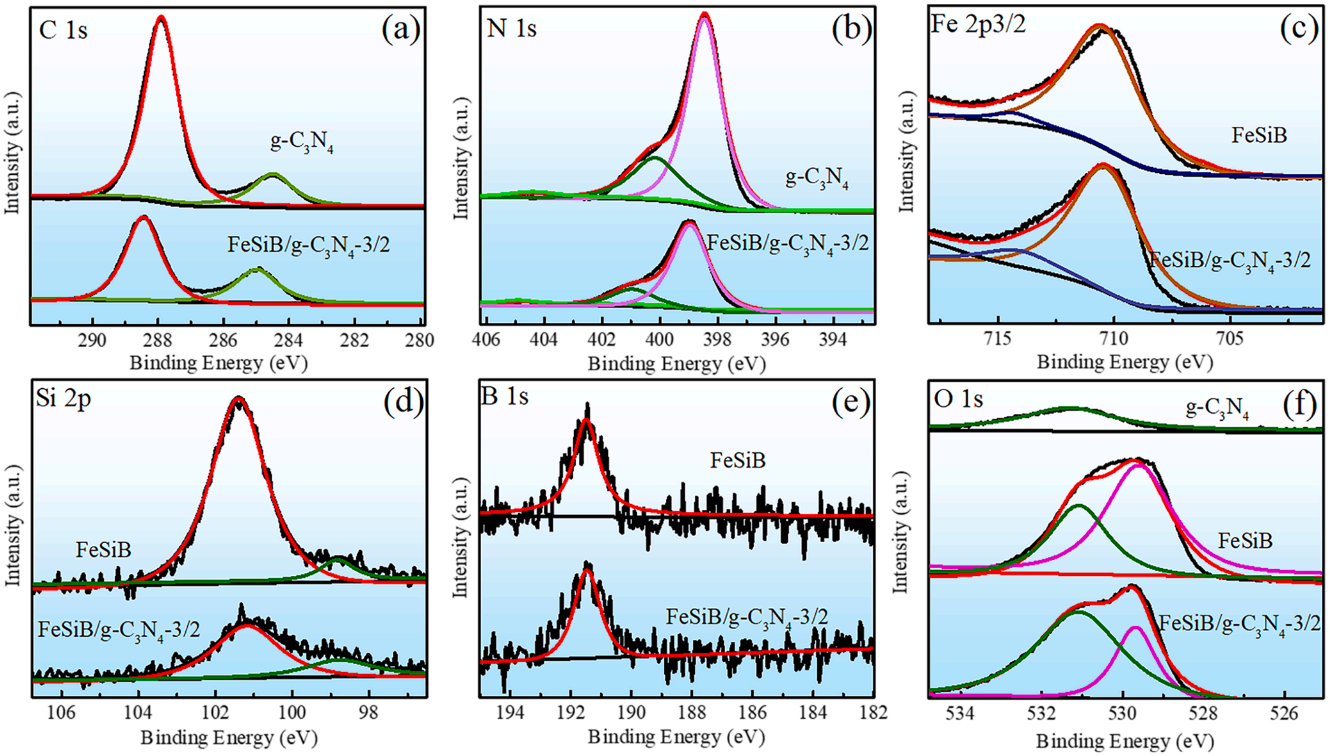

Fig. 8. XPS spectra of g-C_3N_4, FeSiB, and FeSiB/g-C_3N_4-3/2 photocatalysts: (a) C 1 s, (b) N 1 s, (c) Fe 2p3/2, (d) Si 2p, (e) B 1 s, and (f) O 1 s.

positively in FeSiB/g-C_3N_4-3/2 compared with in g-C_3N_4, the electrons from C and N atoms may enrich the electron density around Fe, Si and B atoms [53]. Fig. 8c-f show the XPS spectra of Fe 2p3/2, Si 2p and B 1 s for FeSiB and FeSiB/g-C_3N_4-3 photocatalysts. For Fe 2p3/2 spectrum of FeSiB in Fig. 8c, the peaks are deconvoluted to 710.60 eV and 714.35 eV assigned to the oxidized Fe^{2+}/Fe^{3+} ions [8,13]. For the Si 2p spectrum of FeSiB in Fig. 8d, the two peaks locating at 98.83 eV (Si^0) and 101.38 eV (Si^{4+}) are detected [13]. For B 1 s spectrum of FeSiB in Fig. 8e, one peak

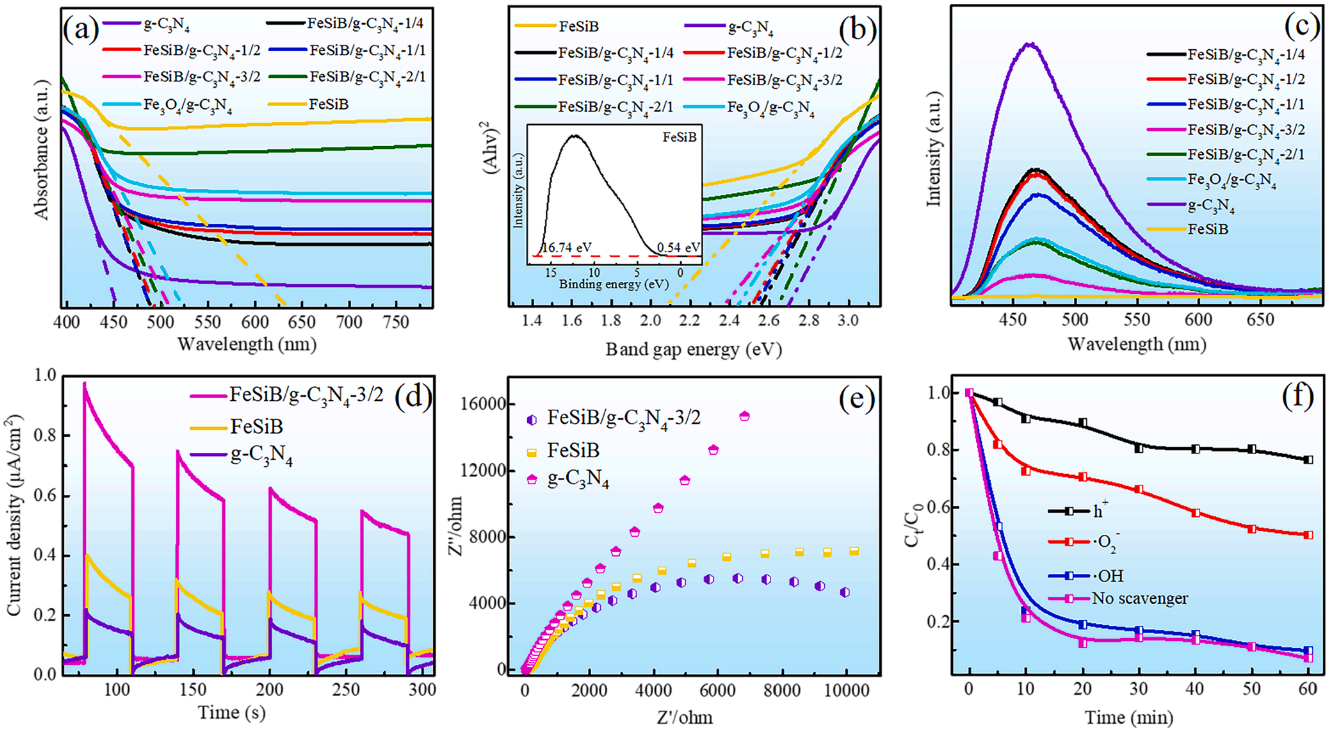

Fig. 9. (a) UV–visible DRS curves of g-C_3N_4, FeSiB, FeSiB/g-C_3N_4-1/4, 1/2, 1/1, 3/2, 2/1 and Fe_3O_4/g-C_3N_4 photocatalysts; (b) $(Ahv)^2$ *vs.* band gap energy (eV), inset is UPS spectrum of FeSiB; (c) PL spectra of g-C_3N_4, FeSiB, FeSiB/g-C_3N_4-1/4, 1/2, 1/1, 3/2, 2/1 and Fe_3O_4/g-C_3N_4 photocatalysts; (d) Electrochemical impedance spectroscopy and (e) transient photocurrent profiles of FeSiB/g-C_3N_4-3/2, FeSiB, and g-C_3N_4; (f) Effect of trapping agents on the degradation efficiency of AO7 solution.

at 191.53 eV is deconvoluted, which come from B^{3+} [8,13]. As the binding energies of Fe 2p3/2 (710.44 eV, 714.30 eV), Si 2p (98.69 eV, 101.18 eV) and B 1 s (191.46 eV) shift negatively in FeSiB/g-C_3N_4-3/2 compared with those in FeSiB, the electrons from C and N atoms may enrich the electron density around Fe, Si and B atoms [53]. The cause of these positive and negative shifts may be that the electronic structure of g-C_3N_4 and FeSiB is altered to develop the heterojunction [54]. Fig. 8f illustrates the XPS spectra of the O 1 s for g-C_3N_4, FeSiB, and FeSiB/g-C_3N_4-3/2 photocatalysts. Only one peak is observed for g-C_3N_4 at 531.30 eV, whereas two peaks are detected at 531.30 eV and 529.87 eV for FeSiB and FeSiB/g-C_3N_4-3/2 photocatalysts. The peak at 531.30 eV can be attributed to the O atoms from O_2 adsorbed on the sample surfaces [55,56]. The peak at 529.87 eV is assigned to oxygen defects [56], indicating that oxygen vacancies are formed on the surfaces of FeSiB/g-C_3N_4-3/2 photocatalyst. The oxygen vacancies after introduction FeSiB into g-C_3N_4 can enhance the optical properties of the material [57,58]. Thereby, the XPS results not only further confirm that the FeSiB/g-C_3N_4-3/2 photocatalyst are successfully prepared, but also uncover that the electronic structure change in the composite boost its photocatalytic activity.

Fig. 9a illustrates the DRS curves of the g-C_3N_4, FeSiB MG, Fe_3O_4/g-C_3N_4 composite and FeSiB/g-C_3N_4 composites. The band gap absorption edge of g-C_3N_4 is around 458 nm, suggesting that only the visible light with a wavelength less than 458 nm can be absorbed by g-C_3N_4. In addition, FeSiB MG powders show a wide range of light absorption up to 632 nm. As expected, all the composites display the absorption capacity of an extended visible light region (488–524 nm), which suggests that composites have superior light absorption capacities than g-C_3N_4. Also, the band gap energies of the samples are estimated from the plots of $(Ahv)^2$ *vs.* band gap energy (eV) [59], as shown in Fig. 9b. It is worth noting that the band gap energies of g-C_3N_4 and FeSiB are about 2.68 eV and 2.09 eV, respectively. Compared with the g-C_3N_4, all composites have narrower band gaps and FeSiB/g-C_3N_4-3/2 has the narrowest band gap (2.37 eV), implying that the FeSiB/g-C_3N_4-3/2 photocatalyst can absorb more visible light to enhance the photocatalytic activity.

Besides, the UPS spectrum of FeSiB was measured and analyzed, as illustrated in the inset of Fig. 9b. According to the linear intersection method, the cut off energy ($E_{\text{cut off}}$) and Fermi energy (E_{Fermi}) of FeSiB are 0.54 eV and 16.74 eV, respectively. Notably, the valence band energy (E_{VB}) is related to the ionization potential (Φ) [60–62], which can be calculated according to Equation (2):

$\Phi = h\nu + E_{\text{cut off}} - E_{\text{Fermi}}$ (2)

where $h\nu$ is the photon energy from He I source as 21.22 eV. Thus, the value of Φ is 5.02 eV for the FeSiB (*vs.* vacuum). Based on the relationship between the vacuum energy and the normal hydrogen electrode (NHE) potential [62], the E_{VB} of FeSiB is calculated to be 0.58 eV (*vs.* NHE). Then the conduction band energy (E_{CB}) of FeSiB is calculated based on Equation (3):

$$\mathrm{E_{CB}} = \mathrm{E_{VB}} - \mathrm{E_g} \tag{3}$$

where E_g is the band gap energy of the semiconductor, E_{CB} and E_{VB} are the conduction band (CB) and valence band (VB) edge potentials, respectively. According to the DRS and UPS spectrum analyses, the band gap energy of FeSiB is about 2.09 eV and the VB of FeSiB is about 0.58 eV, so the CB of FeSiB is −1.51 eV.

PL spectra of all samples have been measured to evaluate the recombination rate of photo-generated electron-hole pairs, whereas the recombination rate is positively correlated to the fluorescence intensity [59,63]. As shown in Fig. 9c, g-C_3N_4 powders exhibit the highest fluorescence intensity, while FeSiB has the lowest fluorescence intensity, and all the composites show much lower fluorescence intensity than g-C_3N_4. It indicates that introduction of FeSiB or Fe_3O_4 into g-C_3N_4 indeed depresses the recombination rate of photo-generated electron-hole pairs. It can be seen that the FeSiB/g-C_3N_4-3/2 composites show the lowest PL fluorescence intensity among all the composites, indicating the lowest recombination rate of electron-hole pairs. In addition to PL analysis, the transient photocurrent response and EIS characterization tests are also executed to investigate the charge migration in the FeSiB/g-C_3N_4-3/2 composite.

Fig. 9d shows the transient photocurrent response of FeSiB, g-C_3N_4, and FeSiB/g-C_3N_4-3/2 samples. All of the three samples can produce photocurrent quickly under UV–visible light irradiation. Nevertheless, the FeSiB/g-C_3N_4-3/2 has the highest generated photocurrent density, while g-C_3N_4 shows the lowest. In general, an improved photocurrent demonstrates the stronger capability in producing and migration of the photo-generated charge carriers under light illumination [64–69]. The data in Fig. 9d indicate that the doped FeSiB improves the photo-conversion efficiency of g-C_3N_4 effectively. A similar result is obtained from the EIS analyses, as shown in Fig. 9e. The smallest arc radius indicates the lowest electron transfer resistance of FeSiB/g-C_3N_4-3/2 among the three samples, which benefits the transport of the photo-excited carriers and results in an improvement of charge separation efficiency [66–68].

3.4. *Active species trapping experiments and mechanism of photocatalytic activity enhancement*

According to previous studies, large quantities of different active species, such as hydroxyl radical (•OH), superoxide radical (•O_2^-) and photo-generated holes (h^+), are involved in the photocatalytic process. To elucidate the photocatalytic mechanism in this work, different scavengers are used during the degradation of AO7 using the FeSiB/g-C_3N_4-3/2 photocatalyst. The changes of AO7 concentration with reaction time using different radical scavengers are shown in Fig. 9f. It is clear that 90% of AO7 is degraded after adding *tert*-butylalcohol (5 mmol L^{-1}) into the photocatalytic reaction solution, which illustrates that •OH does not participate in the degradation of AO7. Only 50% of AO7 is degraded when benzoquinone (5 mmol L^{-1}) is added into the photocatalytic reaction solution, which illustrates that •O_2^- participates in the degradation of AO7. Moreover, the photocatalytic degradation efficiency is significantly inhibited after adding sodium oxalate (5 mmol L^{-1}) into the same degradation, confirming that h^+ plays a critical role in the degradation reaction of AO7. These results confirm that •O_2^- and h^+ play the most important parts in the photocatalytic degradation of AO7 using the FeSiB/g-C_3N_4-3/2 composite.

The higher photocatalytic activity of the FeSiB/g-C_3N_4-3/2 photocatalyst mainly originates from the formation of suitable heterojunction structure between g-C_3N_4 and FeSiB. Under visible-light irradiation, the photo-generated electrons (e^-) continuously transfer from VB to CB in both g-C_3N_4 and FeSiB, leaving holes (h^+) on the VB of both g-C_3N_4 and FeSiB. As metallic FeSiB has higher density of free electrons than g-C_3N_4, a p-n junction (n-FeSiB/p-g-C_3N_4) can be formed in FeSiB/g-C_3N_4-3/2 photocatalyst [70], creating an internal electric field. The n-FeSiB region is positively charged, while the p-g-C_3N_4 region has the negative charge under equilibrium. Thus the photo-generated h^+ flow to the negative pole (p-g-C_3N_4) and the photo-generated e^- move to the positive terminal (n-FeSiB). Besides, the CB of FeSiB (-1.51 eV) is more negative than that of g-C_3N_4 (-1.12 eV), and the VB of g-C_3N_4 (1.56 eV) is more positive than that of FeSiB (0.58 eV). The photo-generated e^- in the CB of FeSiB can migrate to the CB of g-C_3N_4, and the photo-generated h^+ in the VB of g-C_3N_4 can migrate to the VB of FeSiB. Thus, the migration directions of the photo-generated e^- and h^+ in the CB and VB of g-C_3N_4 and FeSiB are opposite to the transfer directions of the e^- and h^+ in the p-n junction. It inevitably leads to a fast combination of the photo-generated electron-hole pairs in the CB of g-C_3N_4 and the VB of FeSiB, which is well known as the Z-scheme recombination [70,71]. Besides, the Z-scheme mechanism is verified by the TEM and EDX analyses of the FeSiB/g-C_3N_4-3/2 sample after photoreduction of Pt. As shown in Fig. 10, more Pt nanoparticles are deposited on the surface of FeSiB than that on g-C_3N_4, which means FeSiB has more electrons in VB to attract the photoreduced Pt. Here we propose Z-scheme charge transfer pathway for FeSiB/g-C_3N_4-3/2 heterojunction [72], where the photo-generated electrons in

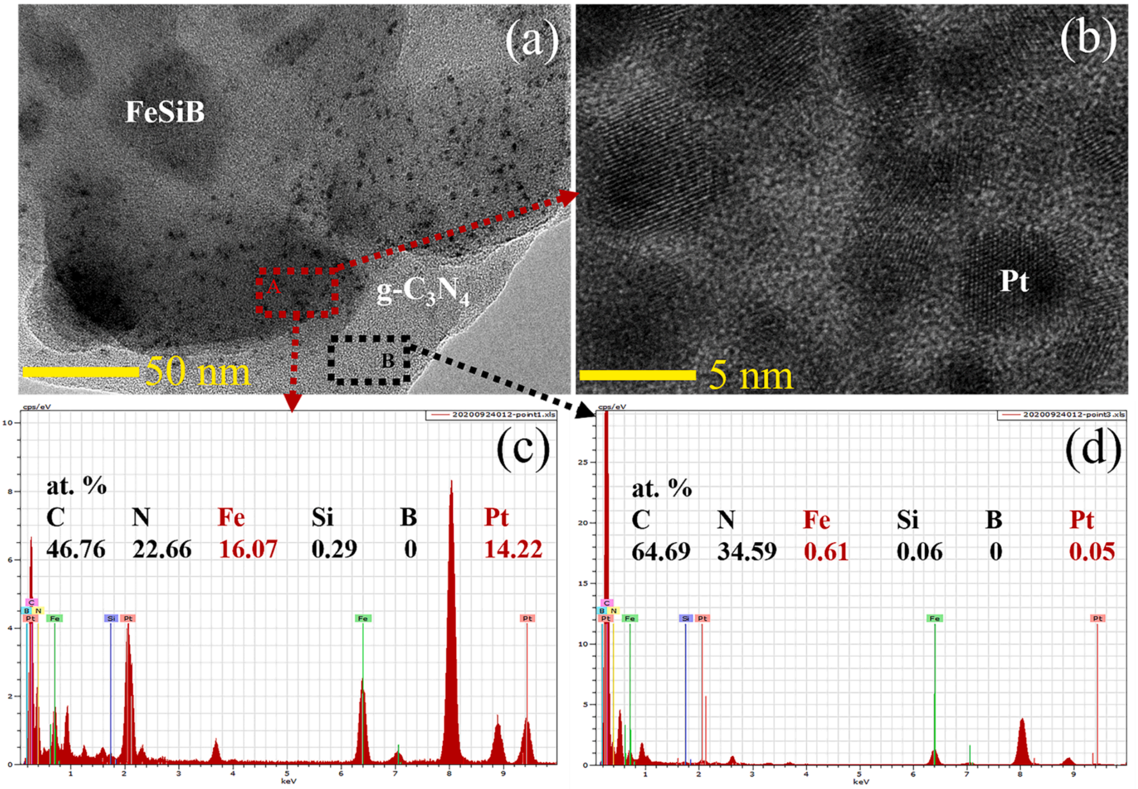

Fig. 10. (a) TEM image for FeSiB/g-C_3N_4-3/2 after photoreduction of Pt, (b) the magnified view of the region A in (a), (c-d) EDX results for the selected region A and B in (a), respectively.

the CB of g-C_3N_4 can transfer to the VB of FeSiB. Then g-C_3N_4 act as the oxidation center due to the accumulation of photo-generated holes, while FeSiB become the photoreduction center.

Based on the above discussion, the photo-generated charge transfer and separation on FeSiB/g-C_3N_4-3/2 composite is proposed and shown in Fig. 11. The photo-generated e^- on CB of g-C_3N_4 transferring to the VB of FeSiB to recombine with h^+ there via the heterojunction interface. Thus, the photo-generated e^- gathers in the CB of FeSiB, while the h^+ stays in the VB of g-C_3N_4, then the separation process of photo-generated electron-hole pairs is improved.

Besides, based on the result from UPS analysis, FeSiB MG has a CB potential (-1.51 eV) that is more negative than $O_2/\bullet O_2^-$ (-0.33 eV) [59,73], suggesting that the accumulated e^- in CB of FeSiB is able to react with O_2 to produce $\bullet O_2^-$, which then oxidizes the AO7 molecules. Meanwhile, the reactions can take place between the e^- in the CB of FeSiB and O_2 to produce H_2O_2 as the CB potential of FeSiB is more negative than that of O_2/H_2O_2 (+0.68 eV), and then the H_2O_2 molecules can react with e^- to produce –OH [74]. Since the VB potential of g-C_3N_4 (1.56 eV) is smaller than those for •OH/–OH (+2.38 eV) and •OH/H_2O (+2.72 eV), the photo-generated h^+ oxidizes the AO7 dye molecules directly instead of reacting with –OH and H_2O to form •OH radicals [74,75]. The above analyses are in good agreement with the findings from the active species trapping experiments, which reveals that $\bullet O_2^-$ and h^+ take charge during the photocatalytic degradation of AO7. Based on the above analyses, the four steps of the photocatalytic degradation of AO7 are illustrated in details as follows:

$FeSiB/g\text{-}C_3N_4 + h\nu \rightarrow FeSiB\ (e^- + h^+) + g\text{-}C_3N_4\ (e^- + h^+)$ (4)

$FeSiB\ (e^- + h^+) + g\text{-}C_3N_4\ (e^- + h^+) \rightarrow FeSiB\ (e^-) + g\text{-}C_3N_4\ (h^+)$ (5)

$FeSiB\ (e^-) + O_2 \rightarrow FeSiB + \bullet O_2^-$ (6)

$\bullet O_2^- + h^+ + AO7 \rightarrow$ degradation products (7)

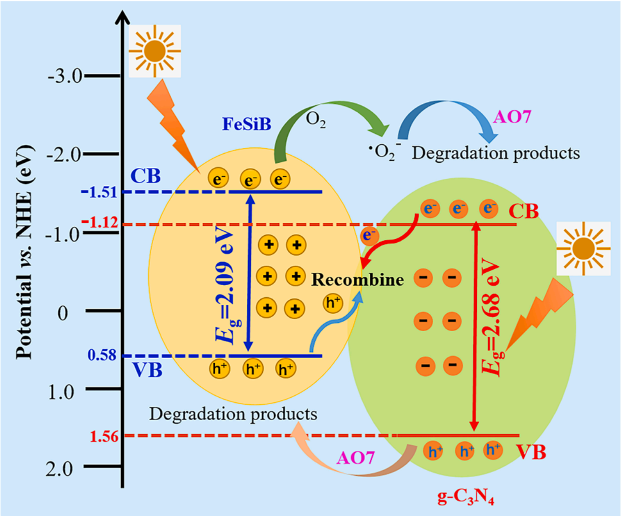

Fig. 11. Mechanism diagram of FeSiB/g-C_3N_4-3/2 photocatalysis. The VB is valence band and CB is conduction band.

Finally, in addition to the charge separation, the specific surface area is also believed to be an important factor for photocatalytic activity [22–24,66,67]. The BET surface areas of the as-synthesized samples are investigated by N_2-adsorption experiments. According to BET analyses, the surface area of FeSiB, g-C_3N_4, FeSiB/g-C_3N_4-1/4, FeSiB/g-C_3N_4-1/2, FeSiB/g-C_3N_4-1/1, FeSiB/g-C_3N_4-3/2, FeSiB/g-C_3N_4-2/1 are 1.0, 6.8, 3.2, 3.1, 2.9, 2.6 and 2.4 m^2/g, respectively. The addition of FeSiB amorphous powders causes only a slight reduction on the surface area of g-C_3N_4. This excludes the possibility that the variation in surface area induces the enhanced charge separation in affecting the photocatalytic process.

4. Conclusion

In summary, the magnetically separable Z-scheme FeSiB/g-C_3N_4 photocatalyst composed of FeSiB MG powders wrapped by g-C_3N_4 are prepared via ball milling. This work provides a magnetically separable photocatalyst that can degrade azo dyes at universal pH conditions. The main conclusions are as follow:

- The FeSiB/g-C_3N_4-3/2 photocatalyst possesses sufficient degrading capability in acidic, neutral and alkaline AO7 solution, and also exhibits excellent reusability. The enhancement of photocatalytic activity of FeSiB/g-C_3N_4 composite can be ascribed to the improved separation efficiency of the photo-generated e^- and h^+.
- The high magnetic saturation of the FeSiB/g-C_3N_4-3/2 photocatalyst allows them to be recycled magnetically.
- The active species trapping experiments confirm that the dominant active species are $\bullet O_2^-$ and h^+ in the photocatalytic process.

CRediT authorship contribution statement

Fang Miao: Conceptualization, Investigation, Writing - original draft. **Qianqian Wang:** Conceptualization, Methodology, Writing - review & editing. **Lai-Chang Zhang:** Validation, Writing - review & editing. **Baolong Shen:** Conceptualization, Supervision, Project administration, Funding acquisition, Writing - review & editing.

Declaration of competing interest

The authors declare that they have no known competing financial interests or personal relationships that could have appeared to influence the work reported in this paper.

Acknowledgements

This work was supported by the National Natural Science Foundation of China (No. 51631003), the Natural Science Foundation of Jiangsu Province of China (Grant No. BK20191269), and the Fundamental Research Funds for the Central Universities (Grant No. 2242019k1G005).

References

[1] L.C. Zhang, Z. Jia, F. Lyu, S.X. Liang, J. Lu, A review of catalytic performance of metallic glasses in wastewater treatment: recent progress and prospects, Prog. Mater. Sci. 105 (2019) 100576.
[2] J. Xu, X. Liu, Z. Cao, W.L. Bai, Q.Y. Shi, Y. Yang, Fast degradation, large capacity, and high electron efficiency of chloramphenicol removal by different carbon-supported nanoscale zerovalent iron, J. Hazard. Mater. 384 (2020) 121253.
[3] K. Villa, J. Parmar, D. Vilela, S. Sánchez, Metal-oxide-based microjets for the simultaneous removal of organic pollutants and heavy metals, Appl. Mater. Interfaces 10 (2018) 20478–20486.
[4] Z. Jia, Q. Wang, L.G. Sun, Q. Wang, L.C. Zhang, G. Wu, J.H. Luan, Z.B. Jiao, A. D. Wang, S.X. Liang, M. Gu, J. Lu, Attractive in situ self-reconstructed hierarchical gradient structure of metallic glass for high efficiency and remarkable stability in catalytic performance, Adv. Funct. Mater. 29 (2019) 1807857.
[5] S.X. Liang, Z. Jia, Y.J. Liu, W.C. Zhang, W.M. Wang, J. Lu, L.C. Zhang, Compelling rejuvenated catalytic performance in metallic glasses, Adv. Mater. 30 (2018) 1802764.
[6] S. Anantharaj, S. Noda, Amorphous catalysts and electrochemical water splitting: an untold story of harmony, Small 16 (2020) 1905779.
[7] S.X. Liang, W.C. Zhang, L.N. Zhang, W.M. Wang, L.C. Zhang, Remediation of industrial contaminated water with arsenic and nitrate by mass-produced Fe-based metallic glass: toward potential industrial applications, Sustain. Mater. Technol. 22 (2019) e00126.
[8] F. Miao, Q.Q. Wang, Q.S. Zeng, L. Hou, T. Liang, Z.Q. Cui, B.L. Shen, Excellent reusability of FeBC amorphous ribbons induced by progressive formation of through-pore structure during acid orange 7 degradation, J. Mater. Sci. Technol. 38 (2020) 107–118.
[9] Z. Jia, J. Kang, W.C. Zhang, W.M. Wang, C. Yang, H. Sun, D. Habibi, L.C. Zhang, Surface aging behaviour of Fe-based amorphous alloys as catalysts during heterogeneous photo Fenton-like process for water treatment, Appl. Catal. B-Environ. 204 (2017) 537–547.
[10] Z. Jia, X.G. Duan, P. Qin, W.C. Zhang, W.M. Wang, C. Yang, H.Q. Sun, S.B. Wang, L. C. Zhang, Disordered atomic packing structure of metallic glass: toward ultrafast hydroxyl radicals production rate and strong electron transfer ability in catalytic performance, Adv. Funct. Mater. 27 (2017) 1702258.
[11] S.X. Liang, X.Q. Wang, W.C. Zhang, Y.J. Liu, W.M. Wang, L.C. Zhang, Selective laser melting manufactured porous Fe-based metallic glass matrix composite with remarkable catalytic activity and reusability, Appl. Mater. Today 19 (2020) 100543.
[12] S.Q. Chen, G.N. Yang, S.T. Luo, S.J. Yin, J.L. Jia, Z. Li, S.H. Gao, Y. Shao, K.F. Yao, Unexpected high performance of Fe-based nanocrystallized ribbons for azo dye decomposition, J. Mater. Chem. A 5 (2017) 14230–14240.
[13] Q.Q. Wang, M.X. Chen, P.H. Lin, Z.Q. Cui, C.L. Chu, B.L. Shen, Investigation of FePC amorphous alloys with self-renewing behaviour for highly efficient decolorization of methylene blue, J. Mater. Chem. A 6 (2018) 10686–10699.
[14] F. Miao, Q.Q. Wang, S.Y. Di, L. Yun, J. Zhou, B.L. Shen, Enhanced dye degradation capability and reusability of Fe-based amorphous ribbons by surface activation, J. Mater. Sci. Technol. 53 (2020) 163–173.
[15] Y.D. Zou, B.B. Yang, Y. Liu, Y. Ren, J.H. Ma, X.R. Zhou, X.W. Cheng, Y.H. Deng, Controllable interface-induced Co-assembly toward highly ordered mesoporous Pt@TiO_2/g-C_3N_4 heterojunctions with enhanced photocatalytic performance, Adv. Funct. Mater. 28 (2018) 1806214.
[16] J.S. Cai, J.Y. Huang, S.C. Wang, J. Iocozzia, Z.T. Sun, J.Y. Sun, Y.K. Yang, Y.K. Lai, Z.Q. Lin, Crafting mussel-inspired metal nanoparticle-decorated ultrathin graphitic carbon nitride for the degradation of chemical pollutants and production of chemical resources, Adv. Mater. 31 (2019) 1806314.
[17] L.R. Kong, X.J. Mu, X.X. Fan, R. Li, Y.T. Zhang, P. Song, F.C. Ma, M.T. Sun, Site-selected N vacancy of g-C_3N_4 for photocatalysis and physical mechanism, Appl. Mater. Today 13 (2018) 329–338.
[18] S.W. Cao, J.X. Low, J.G. Yu, M. Jaroniec, Polymeric photocatalysts based on graphitic carbon nitride, Adv. Mater. 27 (2015) 2150–2176.
[19] A. Mirzaei, Z. Chen, F. Haghighat, L. Yerushalmi, Magnetic fluorinated mesoporous g-C_3N_4 for photocatalytic degradation of amoxicillin: transformation mechanism and toxicity assessment, Appl. Catal. B-Environ. 242 (2019) 337–348.
[20] J. Li, M. Zhang, X. Li, Q.Y. Li, J.J. Yang, Effect of the calcination temperature on the visible light photocatalytic activity of direct contact Z-scheme g-C_3N_4-TiO_2 heterojunction, Appl. Catal. B-Environ. 212 (2017) 106–114.
[21] D. Liu, S. Zhang, J.M. Wang, T.Y. Peng, R.J. Li, Direct Z-Scheme 2D/2D photocatalyst based on ultrathin g-C_3N_4 and WO_3 nanosheets for efficient visible-light-driven H_2 generation, ACS Appl. Mater. Interfaces 11 (2019) 27913–27923.
[22] Q.L. Zhang, P.F. Chen, L. Chen, M.F. Wu, X.Q. Dai, P.X. Xing, H.J. Lin, L.H. Zhao, Y. M. He, Facile fabrication of novel Ag_2S/K-g-C_3N_4 composite and its enhanced performance in photocatalytic $_H$2 evolution, J. Colloid Interf. Sci. 568 (2020) 117–129.
[23] P.F. Chen, L. Chen, S.F. Ge, W.Q. Zhang, M.F. Wu, P.X. Xing, T.B. Rotamond, H. J. Lin, Y. Wu, Y.M. He, Microwave heating preparation of phosphorus doped g-C_3N_4 and its enhanced performance for photocatalytic $_H$2 evolution in the help of A$_g$3P$_O$4 nanoparticles, Int. J. Hydrogen Energ. 45 (2020) 14354–14367.
[24] Z. Feng, L. Zeng, Q.L. Zhang, S.F. Ge, X.Y. Zhao, H.J. Lin, Y.M. He, In situ preparation of g-C_3N_4/$Bi_4O_5I_2$ complex and its elevated photoactivity in Methyl Orange degradation under visible light, J. Environ. Sci. 87 (2020) 149–162.
[25] S. Ye, L.G. Qiu, Y.P. Yuan, Y.J. Zhu, J. Xia, J.F. Zhu, Facile fabrication of magnetically separable graphitic carbon nitride photocatalysts with enhanced photocatalytic activity under visible light, J. Mater. Chem. A 1 (2013) 3008–3015.
[26] M.M. Fang, J.X. Shao, X.G. Huang, J.Y. Wang, W. Chen, Direct Z-scheme $CdFe_2O_4$/g-C_3N_4 hybrid photocatalysts for highly efficient ceftiofur sodium photodegradation, J. Mater. Sci. Technol. 56 (2020) 133–142.
[27] Q.L. Xu, L.Y. Zhang, J.G. Yu, S. Wageh, A.A. Al-Ghamdi, M. Jaroniec, Direct Z-scheme photocatalysts: Principles, synthesis, and applications, Mater. Today 21 (2018) 1042–1063.
[28] M. Jourshabani, B.K. Lee, Z. Shariatinia, From traditional strategies to Z-scheme configuration in graphitic carbon nitride photocatalysts: recent progress and future challenges, Appl. Catal. B-Environ. 276 (2020) 119157.
[29] Y.F. Li, M.H. Zhou, B. Cheng, Y. Shao, Recent advances in g-C_3N_4-based heterojunction photocatalysts, J. Mater. Sci. Technol. 56 (2020) 1–17.
[30] R.A. He, K.Y. Cheng, Z.Y. Wei, S.Y. Zhang, D.F. Xu, Room-temperature in situ fabrication and enhanced photocatalytic activity of direct Z-scheme BiOI/g-C_3N_4 photocatalyst, Appl. Surf. Sci. 465 (2019) 964–972.
[31] L.P. Wang, T.T. Huang, G.P. Yang, C.Y. Lu, F.L. Dong, Y.L. Li, W.S. Guan, The precursor-guided hydrothermal synthesis of $CuBi_2O_4$/WO_3 heterostructure with enhanced photoactivity under simulated solar light irradiation and mechanism insight, J. Hazard. Mater. 381 (2020) 120956.
[32] L.Y. Lu, G.H. Wang, M. Zou, J. Wang, J. Li, Effects of calcining temperature on formation of hierarchical TiO_2/g-C_3N_4 hybrids as an effective Z-Scheme heterojunction photocatalyst, Appl. Surf. Sci. 441 (2018) 1012–1023.
[33] N. Li, Y. Tian, J.H. Zhao, J. Zhang, W. Zuo, L.C. Kong, H. Cui, Z-Scheme 2D/3D g-C_3N_4@ZnO with enhanced photocatalytic activity for cephalexin oxidation under solar light, Chem. Eng. J. 352 (2018) 412–422.
[34] L. Li, C.F. Guo, J.L. Shen, J.Q. Ning, Y.J. Zhong, Y. Hu, Construction of sugar-gourd-shaped CdS/$Co_{1-x}S$ hollow heteronanostructure as an efficient Z-scheme photocatalyst for hydrogen generation, Chem. Eng. J. 400 (2020) 125925.
[35] Z.F. Jiang, B. Wang, Y. Li, H.S. Chan, H.L. Sun, T.Q. Wang, H.M. Li, S.Q. Yuan, M.K. H. Leung, A.H. Lu, P.K. Wong, Solar-light-driven rapid water disinfection by ultrathin magnesium titanate/carbon nitride hybrid photocatalyst: Band structure analysis and role of reactive oxygen species, Appl. Catal. B-Environ. 257 (2019) 117898.

[36] S.X. Liang, Z. Jia, W.C. Zhang, X.F. Li, W.M. Wang, H.C. Lin, L.C. Zhang, Ultrafast activation efficiency of three peroxides by $Fe_{78}Si_9B_{13}$ metallic glass under photo-enhanced catalytic oxidation: a comparative study, Appl. Catal. B-Environ. 221 (2018) 108–118.

[37] J.J. Si, J.L. Gu, H.W. Luan, X.L. Yang, L.X. Shi, Y. Shao, K.F. Yao, Porous composite architecture bestows Fe-based glassy alloy with high and ultra-durable degradation activity in decomposing azo dye, J. Hazard. Mater. 388 (2020) 122043.

[38] X.L. Wang, W.Q. Fang, S. Yang, P.F. Liu, H.J. Zhao, H.G. Yang, Structure disorder of graphitic carbon nitride induced by liquid-assisted grinding for enhanced photocatalytic conversion, RSC Adv. 4 (2014) 10676–10679.

[39] J. Luo, X.S. Zhou, L. Ma, X.Y. Xu, Rational construction of Z-scheme Ag_2CrO_4/g-C_3N_4 composites with enhanced visible-light photocatalytic activity, Appl. Surf. Sci. 390 (2016) 357–367.

[40] L.Q. Ye, J.Y. Liu, Z. Jiang, T.Y. Peng, L. Zan, Facets coupling of BiOBr-g-C_3N_4 composite photocatalyst for enhanced visible-light-driven photocatalytic activity, Appl. Catal. B-Environ. 142 (2013) 1–7.

[41] B. Lin, X.F. Bian, P. Wang, G.P. Luo, Application of Fe-based metallic glasses in wastewater treatment, Mater. Sci. Eng. B-Adv. 177 (2012) 92–95.

[42] Z. Jia, W.C. Zhang, W.M. Wang, D. Habibi, L.C. Zhang, Amorphous $Fe_{78}Si_9B_{13}$ alloy: An efficient and reusable photo-enhanced Fenton-like catalyst in degradation of cibacron brilliant red 3B-A dye under UV–vis light, Appl. Catal. B-Environ. 192 (2016) 46–56.

[43] Y. Tang, Y. Shao, N. Chen, X. Liu, S.Q. Chen, K.F. Yao, Insight into the high reactivity of commercial Fe–Si–B amorphous zero-valent iron in degrading azo dye solutions, RSC Adv 5 (2015) 34032–34039.

[44] Y. Tang, Y. Shao, N. Chen, K.F. Yao, Rapid decomposition of Direct Blue 6 in neutral solution by Fe–B amorphous alloys, RSC Adv. 5 (2015) 6215–6221.

[45] X.Y. Wang, Y.S. Wang, M.C. Gao, J.N. Shen, X.P. Pu, Z.Z. Zhang, H.X. Lin, X. X. Wang, $BiVO_4/Bi_4Ti_3O_{12}$ heterojunction enabling efficient photocatalytic reduction of CO_2 with H_2O to CH_3OH and CO, Appl. Catal. B-Environ. 270 (2020) 118876.

[46] C.M. Gao, T. Wei, Y.Y. Zhang, X.H. Song, Y. Huan, H. Liu, M.W. Zhao, J.H. Yu, X. D. Chen, A photoresponsive rutile TiO2 heterojunction with enhanced electron-hole separation for high-performance hydrogen evolution, Adv. Mater. 31 (2019) 1806596.

[47] J.R. Ran, W.W. Guo, H.L. Wang, B.C. Zhu, J.G. Yu, S.Z. Qiao, Metal-free 2D/2D phosphorene/g-C_3N_4 van der waals heterojunction for highly enhanced visible-light photocatalytic $_H$2 production, Adv. Mater. 30 (2018) 1800128.

[48] D.D. Zhu, Q.X. Zhou, Novel Bi_2WO_6 modified by N-doped graphitic carbon nitride photocatalyst for efficient photocatalytic degradation of phenol under visible light, Appl. Catal. B-Environ. 268 (2020) 118426.

[49] K. Zhu, M.Q. Zhang, X.Y. Feng, L.X. Qin, S.Z. Kang, X.Q. Li, A novel copper-bridged graphitic carbon nitride/porphyrin nanocomposite with dramatically enhanced photocatalytic hydrogen generation, Appl. Catal. B-Environ. 268 (2020) 118434.

[50] G.C. Lei, W.T. Zhao, L.J. Shen, S.J. Liang, C. Au, L.L. Jiang, Isolated iron sites embedded in graphitic carbon nitride (g-C_3N_4) for efficient oxidative desulfurization, Appl. Catal. B-Environ. 267 (2020) 118663.

[51] L. Zhang, Y.Y. Cui, F.L. Yang, Q. Zhang, J.H. Zhang, M.T. Cao, W.L. Dai, Electroless-hydrothermal construction of nickel bridged nickel sulfide@ mesoporous carbon nitride hybrids for highly efficient noble metal-free photocatalytic $_H$2 production, J. Mater. Sci. Technol. 45 (2020) 176–186.

[52] Y.L. Chen, X.Q. Liu, L. Hou, X.R. Guo, R.W. Fu, J.M. Sun, Construction of covalent bonding oxygen-doped carbon nitride/graphitic carbon nitride Z-scheme heterojunction for enhanced visible-light-driven H_2 evolution, Chem. Eng. J. 383 (2020) 123132.

[53] Z. Jia, T. Yang, L.G. Sun, Y.L. Zhao, W.P. Li, J.H. Luan, F.C. Lyu, L.C. Zhang, J. J. Kruzic, J.J. Kai, J.C. Huang, J. Lu, C.T. Liu, A novel multinary intermetallic as an active electrocatalyst for hydrogen evolution, Adv. Mater. 32 (2020) 2000385.

[54] X.J. Wang, Q. Wang, F.T. Li, W.Y. Yang, Y. Zhao, Y.J. Hao, S.J. Liu, Novel BiOCl-C_3N_4 heterojunction photocatalysts: in situ preparation via an ionic-liquid-assisted solvent-thermal route and their visible-light photocatalytic activities, Chem. Eng. J. 234 (2013) 361–371.

[55] Q. Wang, W. Wang, L.L. Zhong, D.M. Liu, X.Z. Cao, F.Y. Cui, Oxygen vacancy-rich 2D/2D BiOCl-g-C_3N_4 ultrathin heterostructure nanosheets for enhanced visible-light-driven photocatalytic activity in environmental remediation, Appl. Catal. B-Environ. 220 (2018) 290–302.

[56] W.X. Zou, B. Deng, X.X. Hu, Y.P. Zhou, Y. Pu, S.H. Yu, K.L. Ma, J.F. Sun, H.Q. Wan, L. Dong, Crystal-plane-dependent metal oxide-support interaction in CeO_2/g-C_3N_4 for photocatalytic hydrogen evolution, Appl. Catal. B-Environ. 238 (2018) 111–118.

[57] J. Ding, Z. Dai, F. Qin, H.P. Zhao, S.A. Zhao, R. Chen, Z-scheme $BiO_{1-x}Br/Bi_2O_2CO_3$ photocatalyst with rich oxygen vacancy as electron mediator for highly efficient degradation of antibiotics, Appl. Catal. B-Environ. 205 (2017) 281–291.

[58] X.N. Hu, Y. Zhang, B.J. Wang, H.J. Li, W.B. Dong, Novel g-C_3N_4/$BiOCl_xI_{1-x}$ nanosheets with rich oxygen vacancies for enhanced photocatalytic degradation of organic contaminants under visible and simulated solar light, Appl. Catal. B-Environ. 256 (2019) 117789.

[59] X.H. Yi, S.Q. Ma, X.D. Du, C. Zhao, H.F. Fu, P. Wang, C.C. Wang, The facile fabrication of 2D/3D Z-scheme g-C_3N_4/UiO-66 heterojunction with enhanced photocatalytic Cr(VI) reduction performance under white light, Chem. Eng. J. 375 (2019) 121944.

[60] Z. Jia, F. Lyu, L.C. Zhang, S. Zeng, S.X. Liang, Y.Y. Li, J. Lu, Pt nanoparticles decorated heterostructured g-C_3N_4/Bi_2MoO_6 microplates with highly enhanced photocatalytic activities under visible light, Sci. Rep. 9 (2019) 7636.

[61] F. Guo, W.L. Shi, C. Zhu, H. Li, Z.H. Kang, CoO and g-C_3N_4 complement each other for highly efficient overall water splitting under visible light, Appl. Catal. B-Environ. 226 (2018) 412–420.

[62] Y.X. Wang, L. Rao, P.F. Wang, Z.Y. Shi, L.X. Zhang, Photocatalytic activity of N-TiO_2/O-doped N vacancy g-C_3N_4 and the intermediates toxicity evaluation under tetracycline hydrochloride and Cr(VI) coexistence environment, Appl. Catal. B-Environ. 262 (2020) 118308.

[63] S. Shanavas, S.M. Roopan, A. Priyadharsan, D. Devipriya, S. Jayapandi, R. Acevedo, P.M. Anbarasan, Computationally guided synthesis of (2D/3D/2D) rGO/Fe_2O_3/g-C_3N_4 nanostructure with improved charge separation and transportation efficiency for degradation of pharmaceutical molecules, Appl. Catal. B-Environ. 255 (2019) 117758.

[64] Z.A. Huang, Q. Sun, K.L. Lv, Z.H. Zhang, M. Li, B. Li, Effect of contact interface between TiO_2 and g-C_3N_4 on the photoreactivity of g-C_3N_4/TiO_2 photocatalyst: (001) vs (101) facets of TiO_2, Appl. Catal. B-Environ. 164 (2015) 420–427.

[65] Y.M. Zheng, Y.Y. Liu, X.L. Guo, Z.T. Chen, W.J. Zhang, Y.X. Wang, X. Tang, Y. Zhang, Y.H. Zhao, Sulfur-doped g-C_3N_4/rGO porous nanosheets for highly efficient photocatalytic degradation of refractory contaminants, J. Mater. Sci. Technol. 41 (2020) 117–126.

[66] Y.M. He, X.Q. Dai, S.N. Ma, L. Chen, Z. Feng, P.X. Xing, J.X. Yu, Y. Wu, Hydrothermal preparation of carbon modified KNb_3O_8 nanosheets for efficient photocatalytic $_H$2 evolution, Ceram. Int. 46 (2020) 11421–11426.

[67] L. Zeng, F. Zhe, Y. Wang, Q.L. Zhang, X.Y. Zhao, X. Hu, Y. Wu, Y.M. He, Preparation of interstitial carbon doped BiOI for enhanced performance in photocatalytic nitrogen fixation and methyl orange degradation, J. Colloid Interf. Sci. 539 (2019) 563–574.

[68] P.X. Xing, W.Q. Zhang, L. Chen, X.Q. Dai, J.L. Zhang, L.H. Zhao, Y.M. He, Preparation of a NiO/$KNbO_3$ nanocomposite via a photodeposition method and its superior performance in photocatalytic $_N$2 fixation, Sustain. Energ. Fuels 4 (2020) 1112–1117.

[69] Y.M. Zheng, Y.Y. Liu, X.L. Guo, W.J. Zhang, Y.X. Wang, M. Zhang, R. Li, Z.B. Peng, H. Xie, Y. Huang, S, Na Co-Doped graphitic carbon nitride/reduced graphene oxide hollow mesoporous spheres for photoelectrochemical catalysis application, ACS Appl. Nano. Mater. 3 (2020) 7982–7991.

[70] W.T. Sun, S.G. Meng, S.J. Zhang, X.Z. Zheng, X.J. Ye, X.L. Fu, S.F. Chen, Insight into the transfer mechanisms of photogenerated carriers for heterojunction photocatalysts with the analogous positions of valence band and conduction band: a case study of ZnO/TiO_2, J. Phys. Chem. C 122 (2018) 15409–15420.

[71] S.G. Meng, W.T. Sun, S.J. Zhang, X.Z. Zheng, X.L. Fu, S.F. Chen, Insight into the transfer mechanism of photogenerated carriers for WO_3/TiO_2 heterojunction photocatalysts: is it the transfer of band-band or Z-Scheme? Why? J. Phys. Chem. C 122 (2018) 26326–26336.

[72] Y.Y. Duan, L. Liang, K.L. Lv, Q. Li, M. Li, TiO_2 faceted nanocrystals on the nanofibers: Homojunction TiO_2 based Z-scheme photocatalyst for air purification, Appl. Surf. Sci. 456 (2018) 817–826.

[73] X. Zhao, X.J. Zhang, B.L. Zhao, F. Jia, D.X. Han, Y.Y. Fan, L. Niu, A. Ivaska, A direct oxygen vacancy essential Z-scheme C@Ti4O$_7$/g-C_3N_4 heterojunctions for visible-light degradation towards environmental dye pollutants, Appl. Surf. Sci. 525 (2020) 146486.

[74] M. Mousavi, A. Habibi-Yangjeh, Magnetically separable ternary g-C_3N_4/Fe_3O_4 /BiOI nanocomposites:novel visible-light-driven photocatalysts based on graphitic carbon nitride, J. Colloid Interf. Sci. 465 (2016) 83–92.

[75] W.L. Shi, F. Guo, S.L. Yuan, In situ synthesis of Z-scheme Ag_3PO_4/$CuBi_2O_4$ photocatalysts and enhanced photocatalytic performance for the degradation of tetracycline under visible light irradiation, Appl. Catal. B-Environ. 209 (2017) 720–728.